

Mixed-stacking few-layer graphene as an elemental weak ferroelectric material

Aitor Garcia-Ruiz,^{*,†,‡} Vladimir Enaldiev,^{†,‡} Andrew McEllistrim,^{†,‡} and
Vladimir I. Fal'ko^{†,‡,¶}

[†]*School of Physics and Astronomy, University of Manchester, Oxford Road, Manchester, M13 9PL, UK*

[‡]*National Graphene Institute, University of Manchester, Oxford Road, Manchester, M13 9PL, UK*

[¶]*Henry Royce Institute for Advanced Materials, University of Manchester, Oxford Road, Manchester, M13 9PL, UK*

E-mail: altor.garcia-ruiz@manchester.ac.uk

Abstract

Ferroelectricity¹ - a spontaneous formation of electric polarisation - is a solid state phenomenon, usually, associated with ionic compounds or complex materials. Here we show that, atypically for elemental solids, few-layer graphenes can host an equilibrium out-of-plane electric polarisation, switchable by sliding the constituent graphene sheets. The systems hosting such effect include mixed-stacking tetralayers and thicker (5-9 layers) rhombohedral graphitic films with a twin boundary in the middle of a flake. The predicted electric polarisation would also appear in marginally (small-angle) twisted few-layer flakes, where lattice reconstruction would give rise to networks of mesoscale domains with alternating value and sign of out-of-plane polarisation.

Keywords: Ferroelectricity; graphene; rhombohedral graphite; twin boundary; twistrionics; screening

Ferroelectricity, a spontaneous electric polarisation in absence of an external electric field, is a phenomenon observed and thoroughly investigated in a broad range of solids²⁻⁴. Caused by charge transfer between constituent atoms in a unit cell, up to now, ferroelectric polarisation was observed only in chemically complex compounds, such as Rochelle salts¹, $\text{Pb}[\text{Zr}_x\text{Ti}_{1-x}]\text{O}_3$ ⁵, BaTiO_3 ⁶, etc...⁷⁻¹¹. Here, we show that there is one exception from this common rule, namely, several structural allotropes of multilayer graphene.

The above statement is based on a theoretical study of various multilayer graphene structures with different stacking orders which, as an elemental material, is non-polar: its intralayer bonding is dominantly covalent, whereas the interlayer adhesion has a van der Waals nature. There are two commonly studied multilayer graphene systems: thin films of Bernal graphite^{12,13} and rhombohedral (ABC) graphite¹⁴. Those two possess inversion symmetry, or $z \rightarrow -z$, respectively, which prohibit spontaneous ferroelectric polarisation. However, graphitic films with mixed Bernal and rhombohedral stackings lack such symmetries, removing constraints on the formation of out-of-plane electric dipole. One example of such a structure is a thin film of rhombohedral graphite with a twin boundary inside it¹⁵, which consists of two ABC parts with n and m layers ($n \neq m$), rotated by 180° with respect to each other, held together by an ABA-trilayer (see Fig. 1).

In the following section, we study $n\text{ABAm}$, with $n \neq m$, and demonstrate that they exhibit a weak spontaneous out-of-plane electric polarisation, P_z , at zero doping. We determine the roles of parameters in the full multi-parameter Slonczewski-Weiss-McClure (SWMcC) Hamiltonian that are related to the asymmetries that permit a finite P_z . Importantly, we find that self-consistently implemented screening of internal electric field not only strongly reduces P_z magnitude, but also changes its sign for some structures, which is a result of different inter-layer charge redistributions, caused individually by each symmetry-breaking term in the bare SWMcC Hamiltonian. To mention, for tetralayers, the known values and signs of SWMcC parameters¹⁶ are such that the largest contributions they produced individually mostly cancel each other, making the result sensitive to the precise choice of parameters. At the same time, for marginally twisted tetralayers, where lattice relaxation leads to the formation of equilibrium stacking domains (where polarisation is small), the

domain walls host seeds of different stacking arrangements for which such cancellation does not occur leading to an order of magnitude larger local P_z values.

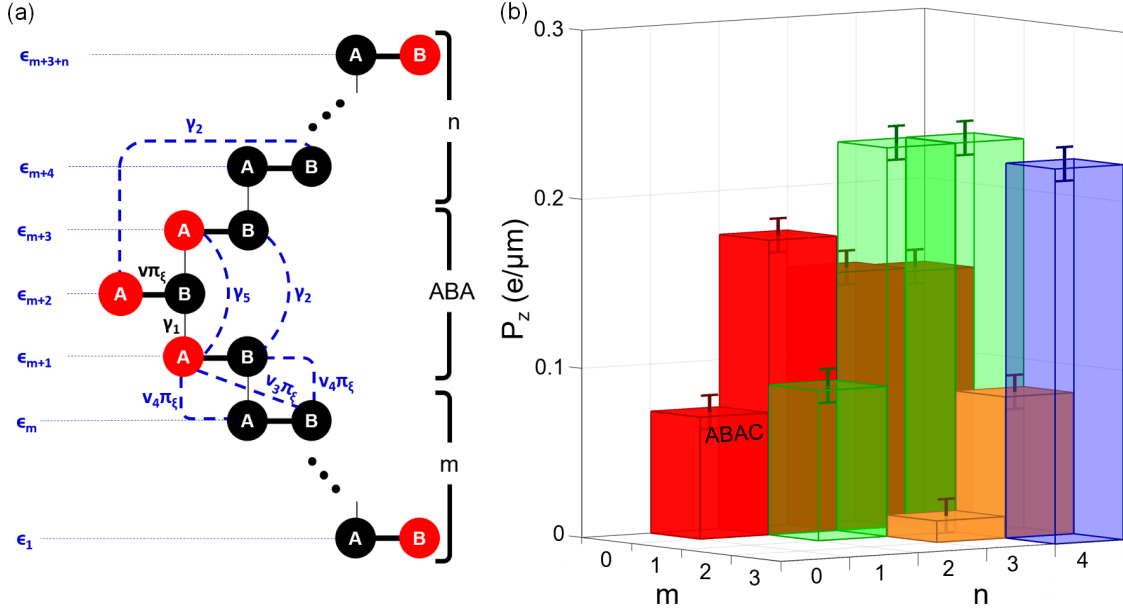


Figure 1: Sketch of a twinned rhombohedral graphitic film, highlighting in dashed lines the SWMcC couplings, with a radius proportional to the number of dimmer bonds and showing in red the low-energy orbitals (three non-dimer bonds and the anti-symmetric combination of A-sublattice orbitals of the layers adjacent to the twin boundary). The right panel show the dependence of the ferroelectric polarisation density as a function of thicknesses n and m of twinned layers.

Below, we use a full Slonczewski-Weiss-McClure (SWMcC) model of graphite films discussed in Ref.¹⁵. This model accounts for couplings sketched in Fig. 1, which include both the closest and next-neighbour hoppings, and it is implemented in the framework of a hybrid $\mathbf{k} \cdot \mathbf{p}$ -tight-binding model¹⁷, using a Hamiltonian, \mathcal{H} , specified in the Supplementary Materials. The diagonalisation of \mathcal{H} gives the dispersions, $\varepsilon_\beta(\mathbf{p})$, and wavefunctions, $\psi_{\beta,\mathbf{p}}^{\alpha L}$, of bands β in the multilayer, which we use to compute both on-layer electron densities, n_L , and electric polarisation:

$$P_z = ed \sum_{L=1}^{n+m+3} L n_L; \quad n_L = 4 \sum_{\beta, \alpha L, \mathbf{p}} \left[|\psi_{\beta,\mathbf{p}}^{\alpha L}|^2 \Theta[E_F - \varepsilon_\beta(\mathbf{p})] - \frac{1}{4} \right]. \quad (1)$$

Here e is the electron charge, $d \approx 3.35 \text{ \AA}$ the interlayer distance, and “ L ” the layer index, and

$\alpha_L = A_L, B_L$ sublattice indices. When computing the electron densities, n_L , we take account for the screening the potential they generate on each individual layer, as

$$\epsilon_i - \epsilon_{i-1} = \frac{e^2 d}{2\epsilon_0} \left[(n_i - n_{i-1}) \frac{1 + \epsilon_z}{2\epsilon_z} + \sum_{j>i} \frac{n_j}{\epsilon_z} - \sum_{j'<i-1} \frac{n_{j'}}{\epsilon_z} \right], \quad (2)$$

where $\epsilon_z \approx 2.6$ is an effective out-of-plane dielectric permittivity of graphene stacks determined by the polarizability of carbon atoms¹⁸.

Among all SWMcC couplings, next-neighbour hoppings γ_2, γ_5 and v_4 , together with the energy difference between dimer and non-dimer sites, Δ' , are most important for a non-zero value of the ferroelectric polarisation, P_z , to form across the structure. This is because such couplings break a hidden electron-hole symmetry¹, $\mathcal{U}\mathcal{H}\mathcal{U}^\dagger = -\mathcal{H}$ ($\mathcal{U} = \hat{1}_{n+3+m} \otimes \sigma_z$ is a unitary matrix equal to direct product of $n + 3 + m$ -rank identity and third Pauli matrices, respectively), characteristic of the 'reduced' models of graphenes limited to the closest neighbour couplings only. To mention, the on-layer potentials in Eq. (2) induced by the screening can also break all symmetries, which will be important for understanding the result of self-consistent analysis.

For a detailed quantitative self-consistent analysis of spontaneous electric polarisation P_z , we implement the following steps. First, we compute the electric polarisation induced by one of the four symmetry-breaking terms in SWMcC Hamiltonian for each of the considered structures, both with and without self-consistent implementation of screening. Then, we check that the cumulative effect of all the terms in the full SWMcC model can be approximation as a sum of the individual symmetry-breaking contributions as

$$P_z = \left(\mathcal{X}_4 \frac{v_4}{v} \gamma_1 + \mathcal{X}_D \Delta' + \mathcal{X}_2 \gamma_2 + \mathcal{X}_5 \gamma_5 \right) \frac{|\gamma_1|}{\hbar^2 v^2} \cdot ed. \quad (3)$$

Here, $\mathcal{X}_{4,D,2,5}$ are dimensionless factors which values for the ABCB tetralayer are listed in Table

¹Applying \mathcal{U} to Hamiltonian, $\mathcal{U}\mathcal{H}\mathcal{U}^\dagger$, we change signs all of its matrix elements except those on the diagonal of matrices $H_g^{s,b}, V, W$, and \tilde{W} being proportional to either of the parameters $v_4, \Delta', \gamma_2, \gamma_5$. Therefore, for $v_4 = \Delta' = \gamma_2 = \gamma_5 = 0$ Hamiltonian possesses the hidden electron-hole symmetry $\mathcal{U}\mathcal{H}\mathcal{U}^\dagger = -\mathcal{H}$, which results in $P_z = 0$. This is because at zero doping polarisations given by electron and hole parts of spectrum should be opposite, whereas the electron-hole symmetry equalizes them requiring zero value for both.

Table 1: Numerical values for the parameters \mathcal{X} in Eq. (3), and their contribution towards the polarisation, with and without including the screening effects of on-layer charge redistribution. In the last four rows we also include the on-layer potentials. To evaluate the dependence with respect to each parameter, we use a Hamiltonian model where all other SWMcC parameters were set to zero except $v = 1.02 \cdot 10^6$ m/s and $\gamma_1 = 390$ meV.

	$\frac{P_z^u}{e/\mu\text{m}}$	Coeffs.			$\frac{P_z}{e/\mu\text{m}}$	$\frac{\epsilon_2 - \epsilon_1}{\text{meV}}$	$\frac{\epsilon_3 - \epsilon_2}{\text{meV}}$	$\frac{\epsilon_4 - \epsilon_3}{\text{meV}}$
Total	0.50				-0.07			
$v_4 = 0.022v$	0.09	0.036	\mathcal{X}_4	0.009	0.02	-1.332	1.323	-0.418
$\Delta' = 25$ meV	-0.33	-0.045	\mathcal{X}_D	-0.032	-0.23	-5.607	5.631	0.716
$\gamma_2 = -17$ meV	0.28	-0.058	\mathcal{X}_2	0.016	-0.08	1.403	-1.959	2.158
$\gamma_5 = 38$ meV	0.45	0.041	\mathcal{X}_5	0.019	0.21	1.498	-1.567	-1.404
	unscreened	self-consistently screened						

1.

Accounting for the charge redistribution self-consistently is an important part of the presented calculations. Taking into account redistribution of charges produced by screening of electric fields attributed to polarisation not only reduces the value of P_z by one order of magnitude, but also can change the sign of some of the individual symmetry-breaking contributions, when compared with the unscreened case. We investigate numerically this effect by comparing the values for \mathcal{X} in ABCB graphenes, with and without the self-consistent implementation of screening in Table 1. In absence of screening ($\epsilon_i = 0$), we obtain a value of $P_z \approx 0.5$ e/ μm , whereas implementing screening changes this values to $P_z = -0.07$ e/ μm . This is because the two largest contributions to the ferroelectric polarisation, coming from \mathcal{X}_D and \mathcal{X}_2 , have opposite signs and nearly cancel each other for the choice of SWMcC based on Ref.¹⁶, leaving γ_2 to define the value of P_z , so that the overall result changes sign after the implementation of screening. We suggest that such a sensitivity of the computed values of P_z to the input SWMcC parameters may be used to further narrow down their choices by comparing the computed P_z with the experimentally measured polarisation of tetralayers. We find that screening is equally important for the analysis of polarisation in thicker films, though the above-mentioned cancellation does not occur for all thicknesses. In Fig. 1, we show the computed values of P_z in various nABAm structures with $m > n$ (the mirror-symmetric mABAn configurations have the same magnitude of P_z but opposite sign).

While the above-described twinned rhombohedral graphitic films may appear naturally among flakes exfoliated from bulk material, one can try to build weakly ferroelectric multilayers by a twistrionic assembly of thinner flakes^{19–23}. A small misalignment of crystalline axes of the assembled graphene flakes, unavoidable in the mechanical transfer, leads to a long period variation of stacking, known as moiré structure, which upon the lattice relaxation (promoting energetically preferred local stacking order) results in a network of domains with AB and BA interlayer preferences at the twisted interface.

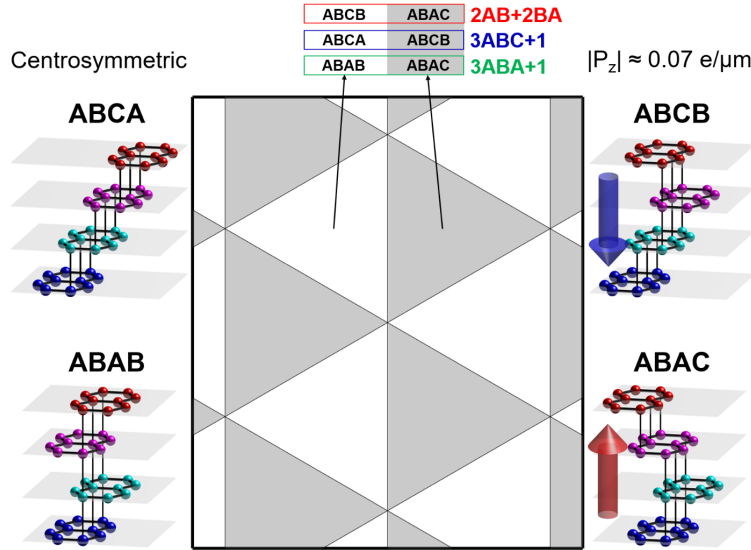


Figure 2: An array of triangular domains in a marginally twisted tetralayer graphene ($2AB+2BA$, $3ABA+1$ and $3ABC+1$), which we expect to form by lattice reconstruction of a long-period moiré superlattice. Domain stackings with and without ferroelectric charge transfer for various twisted tetralayer structures are shown on the right and left hand side sketches, respectively.

Here, we consider structures with graphene monolayer small-angle-twisted with respect to Bernal and rhombohedral trilayer graphene ($3ABA+1$ and $3ABC+1$, respectively) and a twisted double-bilayer ($2AB+2BA$). At the twisted interface, moiré superlattice undergoes lattice reconstruction promoting formation of triangular domain arrays with local AB and BA stackings, shown in Fig. 2, which are separated by network of domain walls (DWs). We model lattice reconstruction in the structures following an approach of Refs.^{24,25}, find local deformations of lattices in top/bottom flakes, $\mathbf{u}_{t/b}$, that minimise (via domain formation) a sum of elastic and interlayer

adhesion energies (see Supplementary Materials).

Then, we find ferroelectric polarisation of small-angle twisted structures using local stacking approximation. That is, we calculate the polarisation based on a Hamiltonian shown in Methods, describing aligned tetralayer films with an in-plane offset $\mathbf{r}_0 = \theta \hat{z} \times \mathbf{r} + \mathbf{u}_t - \mathbf{u}_b$ between constituent parts. As a reference, we set $\mathbf{r}_0 = 0$ for ABBA-stacking in 2AB+2BA, ABAA-stacking in 3ABA+1, and ABCC-stacking in 3ABC+1 areas. Having calculated P_z with a self-consistent analysis of screening and on a sufficiently dense grid of interlayer offsets \mathbf{r}_0 , we interpolate it in the form of a harmonic series,

$$P_z(\mathbf{r}_0) = \sum_{\Lambda=0}^{+\infty} \sum_{j=0}^2 \sum_{s=\pm} [A_{\Lambda} \sin(\mathbf{G}_{\Lambda}^{j,s} \mathbf{r}_0) + B_{\Lambda} \cos(s \mathbf{G}_{\Lambda}^{j,s} \mathbf{r}_0)],$$

$$\mathbf{G}_{\Lambda}^{j,s} = \frac{4\pi}{a\sqrt{3}} \begin{pmatrix} \lambda_1 \sin\left(\frac{2\pi}{3}\left(j + \frac{s}{2}\right)\right) - \lambda_2 \sin\left(\frac{2\pi}{3}j\right) \\ -\lambda_1 \cos\left(\frac{2\pi}{3}\left(j + \frac{s}{2}\right)\right) + \lambda_2 \cos\left(\frac{2\pi}{3}j\right) \end{pmatrix}, \quad (4)$$

where Λ labels reciprocal lattice vectors of graphene in the ascending order of the lengths (see Table 2). Note that mirror reflection of AB and BA bilayers in 2AB+2BA films translates to symmetry properties of $P_z(\mathbf{r}_0)$. In particular, for a reference frame with x -axis along zigzag and y -axis along armchair, $P_z(x_0, y_0) = P_z(-x_0, y_0)$, as zigzag axis is perpendicular to vertical mirror symmetry plane conserving P_z , and, $P_z(x_0, y_0) = -P_z(x_0, -y_0)$, as mirror reflection in armchair axis is equivalent to exchange of AB \leftrightarrow BA stackings in each bilayer and consequently leads to inversion of P_z . This requires $B_{\Lambda} = 0$ in (4) for 2AB+2BA films, whereas the other Fourier coefficients are listed in Table 2.

In Fig. 3, we illustrate the resulting real space distributions of the ferroelectric polarisation in a representative region of moiré superlattice for each of the considered tetralayer films. The mirror reflection in armchair axes prescribe zero polarisation for DWs in 2AB+2BA films, shown in Fig. 2, oriented along armchair crystallographic axes and separating domains with opposite polarisation $P_z = \pm 0.07e/\mu\text{m}$. This would correspond to the transfer of $\sim 10^{11} \text{ cm}^{-2}$ electron density between the tetralayer film surfaces. Note that close to domain corners polarisation reverses sign and its

magnitude become four times higher than those in the middle of domains.

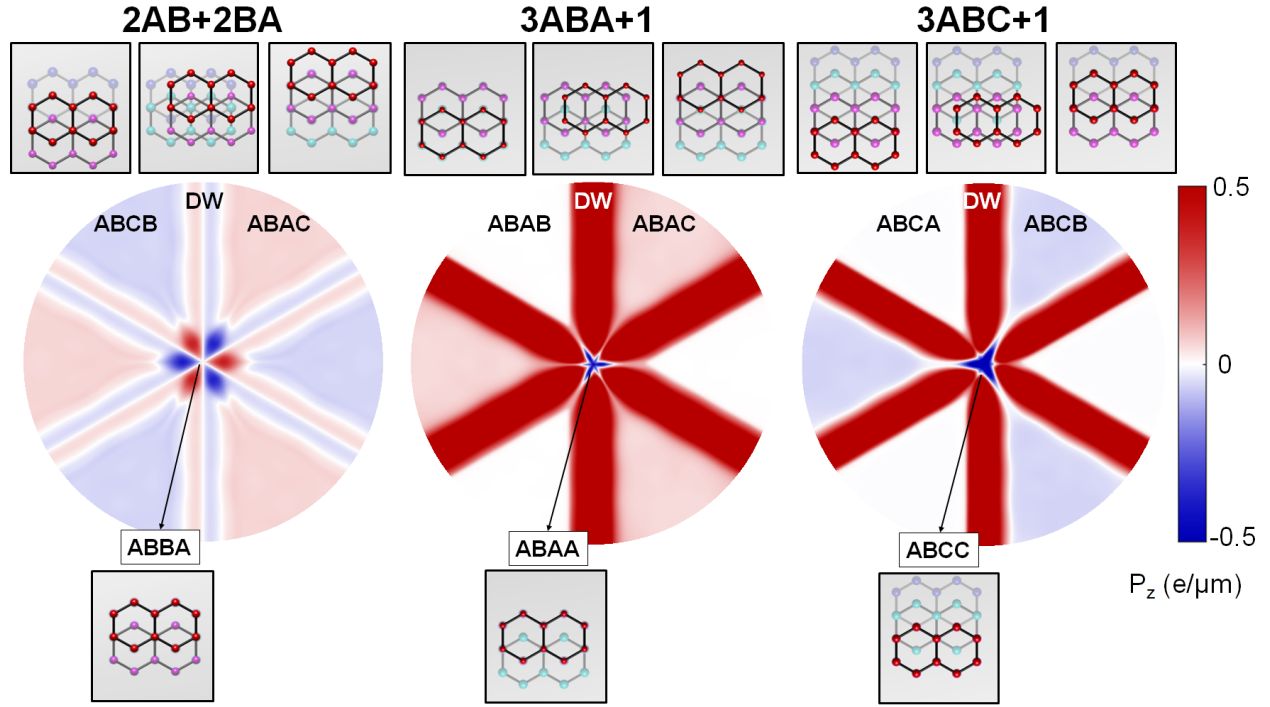


Figure 3: Ferroelectric polarisation around a circular area of $1 \mu\text{m}$ of diameter, centred at the intercross of triangular networks of domain walls, shown in Fig. 2. The inset represent the top view of the local stacking configuration at the domains, the domain walls and the centre of the intercross of triangular network of domain walls.

DW intercrossings possessing opposite polarisation compared to the inner part of DW. In contrast, supercells of $3\text{ABA}+1$ ($3\text{ABC}+1$) twisted tetralayers contain one inversion symmetric domain, ABAB (ABCA) (see Fig. 2), where ferroelectric polarisation is forbidden by symmetry and another, ABAC (ABCB) domain (as in $2\text{AB}+2\text{BA}$ films), which carries an out-of-plane polarisation. We note that in $3\text{ABA}+1$ ($3\text{ABC}+1$) tetralayers DWs and their intercrossings host even an order of magnitude stronger local vertical charge transfer than in the inner areas of the domains.

The spontaneous out-of-plane polarisation that we predict here for few-layer rhombohedral graphene structures is a feature induced by an asymmetrically placed twin boundary which breaks inversion and mirror symmetry in the system, and we trace it to the effect of individual terms in the full Sloczewski-Weiss-McClure model of graphite involved with such asymmetries and responsible for electron-hole symmetry breaking of the single-particle spectra.

Table 2: Coefficients of the Fourier expansion in Eq. (4) for the three stacking configurations analysed.

Λ	$\{\lambda_1, \lambda_2\}$	AB+BA	ABA+1		ABA+1	
		A_Λ ($e/\mu\text{m}$)	A_Λ ($e/\mu\text{m}$)	B_Λ ($e/\mu\text{m}$)	A_Λ ($e/\mu\text{m}$)	B_Λ ($e/\mu\text{m}$)
0	{0, 0}	-	-	0.0384	-	0.0243
1	{1, 0}	0.0626	-0.0293	-0.1231	0.0488	-0.1599
2	{2, 1}	0	0	-0.0917	0	-0.1015
3	{2, 0}	0.0847	-0.0320	0.0927	0.0621	0.0946
4	{3, 1}	0.0147	-0.0045	-0.0319	0.0096	-0.0369
5	{3, 0}	0	-0.0067	0.0307	0.0015	0.0140
6	{4, 2}	0	0	-0.0335	0	-0.0208
7	{4, 1}	0.0118	-0.0039	0.0151	0.0052	0.0083
8	{4, 0}	0.0076	-0.0057	0.0024	0.0102	-0.0036
9	{5, 2}	0.0015	0.0013	-0.0130	-0.0021	-0.0118
10	{5, 1}	-0.0002	-0.0017	0.0189	0.0001	0.0013
11	{5, 0}	0.0062	-0.0025	0.0158	0.0032	0.0009
12	{6, 3}	0	0	-0.0151	0	-0.0060
13	{6, 2}	0.0013	0.0004	0.0033	-0.0005	-0.0002
14	{6, 1}	0.0035	-0.0025	0.0011	0.0041	-0.0014
15	{6, 0}	-0.0004	-0.0001	0.0042	-0.0002	-0.0024
16	{7, 3}	0.0009	0.0023	-0.0071	-0.0026	-0.0046
17	{7, 2}	0.0001	-0.0010	0.0036	-0.0001	-0.0007
18	{7, 1}	0.0024	-0.0007	0.0015	0.0013	-0.0004
19	{8, 4}	0	0	-0.0081	0	-0.0025
20	{7, 0}	0.0019	-0.0014	0.0012	0.0018	-0.0006

The reported calculations show that the size and orientation of P_z are critically affected by the intrinsic screening inside the graphitic films, leading to the opposite signs of P_z in tetralayers analysed with and without screening, and much smaller values, about one order of magnitude smaller than those experimentally reported in WTe_2 ²⁶, MoS_2 ¹¹ or hBN ²⁷. We also note that in marginally twisted multilayers, the largest local polarisation appears to be at domain walls and the near the nodes of domain wall networks. Overall, such sensitivity to the choice of the values of input parameters in the tight-binding model of graphite, number of layers in the film and variation across the moiré pattern in marginally twisted structures may be used to experimentally refine the parametrization of Sloczewski-Weiss-McClure model.

Acknowledgement

This work was supported by EC-FET Core 3 European Graphene Flagship Project, EC-FET Quantum Flagship Project 2D-SIPC, EPSRC grants EP/S030719/1 and EP/V007033/1, and the Lloyd Register Foundation Nanotechnology Grant.

Supporting Information Available

In the file “ Supporting_Information.pdf”, we describe the methods used to produce the data of the text, including:

- Description of the Hamiltonian of rhombohedral graphite with a twin boundary
- Description of the Hamiltonian of tetralayer graphite with one interface laterally shifted by an arbitrary amount r_0
- Analysis of the area in reciprocal space required for convergence.
- Description of the method used to account for electrostatic screening.
- Analysis of the dependence of P_z and P_z^u on each of the SWMcC parameters.
- Description of the method used to account for lattice relaxation.

Author contributions

V. F. conceived the project. A. G.-R. made calculations of band structures, ferroelectric polarization, self-consistent implementation of screening and prepared all figures in the text. V. E. did analysis of lattice reconstruction. All the authors discussed the results and wrote the manuscript.

Competing Interests

The Authors declare no competing financial or non-financial interests.

Data availability

The data that support the plots in the manuscript are available from the corresponding authors upon reasonable request.

References

- (1) Valasek, J. Piezo-Electric and Allied Phenomena in Rochelle Salt. *Phys. Rev.* **1921**, *17*, 475–481.
- (2) Lines, M. E.; Glass, A. M. *Principles and Applications of Ferroelectrics and Related Materials*; Oxford University Press, 1977.
- (3) Uchido, K. *Ferroelectric devices*; CRC Press, 2010.
- (4) Bain, A. K.; Chand, P. *Ferroelectrics: Principles and Applications*; Wiley-VCH, 2017.
- (5) Jaffe, B.; Roth, R. S.; S., M. Piezoelectric Properties of Lead Zirconate-Lead Titanate Solid-Solution Ceramics. *J. App. Physics* **1954**, *25*, 809.
- (6) Megaw, H. D. Origin of ferroelectricity in barium titanate and other perovskite-type crystals. *Acta Crystallographica* **1952**, *15*, 739–749.
- (7) Chang, K.; Liu, J.; Lin, H.; Wang, N.; Zhao, K.; Zhang, A.; Jin, F.; Zhong, Y.; Hu, X.; Duan, W.; Zhang, Q.; Fu, L.; Xue, Q.-K.; Chen, X.; Ji, S.-H. Discovery of robust in-plane ferroelectricity in atomic-thick SnTe. *Science* **2016**, *353*, 274–278.

- (8) de la Barrera, S. C.; Cao, Q.; Gao, Y.; Gao, Y.; Bheemarasetty, V. S.; Yan, J.; Mandrus, D. G.; Zhu, W.; Xiao, D.; Hunt, B. M. Direct measurement of ferroelectric polarization in a tunable semimetal. *Nature Communications* **2021**, *12*, 5298.
- (9) Sharma, P.; Xiang, F.-X.; Shao, D.-F.; Zhang, D.; Tsymbal, E. Y.; Hamilton, A. R.; Seidel, J. A room-temperature ferroelectric semimetal. *Science Advances* **2019**, *5*, eaax5080.
- (10) Fei, Z.; Zhao, W.; Palomaki, T. A.; Sun, B.; Miller, M. K.; Zhao, Z.; Yan, J.; Xu, X.; Cobden, D. H. Ferroelectric switching of a two-dimensional metal. *Nature* **2018**, *560*, 336–339, Number: 7718 Publisher: Nature Publishing Group.
- (11) Weston, A. et al. Interfacial ferroelectricity in marginally twisted 2D semiconductors. *Nature Nanotechnology* **2022**, *17*, 390–395.
- (12) Bernal, J. D. The structure of Graphite. *Proc. R. Soc. Lond. A* **1924**, 749–773.
- (13) FREISE, E. J. Structure of Graphite. *Nature* **1962**, *193*, 671–672.
- (14) Latychevskaia, T.; Son, S.-K.; Yang, Y.; Chancellor, D.; Brown, M.; Ozdemir, S.; Madan, I.; Berruto, G.; Carbone, F.; Mishchenko, A.; Novoselov, K. S. Stacking transition in rhombohedral graphite. *Frontiers of Physics* **2018**, *14*, 13608.
- (15) Garcia-Ruiz, A.; Slizovskiy, S.; Fal’ko, V. I. Flat Bands for Electrons in Rhombohedral Graphene Multilayers with a Twin Boundary. *Advanced Materials Interfaces* **2023**, *10*, 2202221.
- (16) Yin, J. et al. Dimensional reduction, quantum Hall effect and layer parity in graphite films. *Nature Physics* **2019**, *15*, 437–442.
- (17) Garcia-Ruiz, A.; Deng, H.-Y.; Enaldiev, V. V.; Fal’ko, V. I. Full Slonczewski-Weiss-McClure parametrization of few-layer twistrionic graphene. *Phys. Rev. B* **2021**, *104*, 085402.
- (18) Slizovskiy, S.; Garcia-Ruiz, A.; Berdyugin, A. I.; Xin, N.; Taniguchi, T.; Watanabe, K.; Geim, A. K.; Drummond, N. D.; Fal’ko, V. I. Out-of-Plane Dielectric Susceptibility of

- Graphene in Twistrionic and Bernal Bilayers. *Nano Letters* **2021**, *21*, 6678–6683, PMID: 34296602.
- (19) Kim, K.; Yankowitz, M.; Fallahazad, B.; Kang, S.; Movva, H. C. P.; Huang, S.; Larentis, S.; Corbet, C. M.; Taniguchi, T.; Watanabe, K.; Banerjee, S. K.; LeRoy, B. J.; Tutuc, E. van der Waals Heterostructures with High Accuracy Rotational Alignment. *Nano Letters* **2016**, *16*, 1989–1995, PMID: 26859527.
- (20) Caldwell, J. D.; Anderson, T. J.; Culbertson, J. C.; Jernigan, G. G.; Hobart, K. D.; Kub, F. J.; Tadjer, M. J.; Tedesco, J. L.; Hite, J. K.; Mastro, M. A.; Myers-Ward, R. L.; Eddy, C. R. J.; Campbell, P. M.; Gaskill, D. K. Technique for the Dry Transfer of Epitaxial Graphene onto Arbitrary Substrates. *ACS Nano* **2010**, *4*, 1108–1114, Publisher: American Chemical Society.
- (21) Kim, K.; DaSilva, A.; Huang, S.; Fallahazad, B.; Larentis, S.; Taniguchi, T.; Watanabe, K.; LeRoy, B. J.; MacDonald, A. H.; Tutuc, E. Tunable moiré bands and strong correlations in small-twist-angle bilayer graphene. *Proceedings of the National Academy of Sciences* **2017**, *114*, 3364–3369.
- (22) Xu, S. et al. Tunable van Hove singularities and correlated states in twisted monolayer–bilayer graphene. *Nature Physics* **2021**, *17*, 619–626.
- (23) Tomić, P.; Rickhaus, P.; Garcia-Ruiz, A.; Zheng, G.; Portolés, E.; Fal’ko, V.; Watanabe, K.; Taniguchi, T.; Ensslin, K.; Ihn, T.; de Vries, F. K. Scattering between Minivalleys in Twisted Double Bilayer Graphene. *Phys. Rev. Lett.* **2022**, *128*, 057702.
- (24) Nam, N. N. T.; Koshino, M. Lattice relaxation and energy band modulation in twisted bilayer graphene. *Phys. Rev. B* **2017**, *96*, 075311.
- (25) Enaldiev, V. V.; Zólyomi, V.; Yelgel, C.; Magorrian, S. J.; Fal’ko, V. I. Stacking Domains and Dislocation Networks in Marginally Twisted Bilayers of Transition Metal Dichalcogenides. *Phys. Rev. Lett.* **2020**, *124*, 206101.

- (26) Fei, Z.; Zhao, W.; Palomaki, T. A.; Sun, B.; Miller, M. K.; Zhao, Z.; Yan, J.; Xu, X.; Cobden, D. H. Ferroelectric switching of a two-dimensional metal. *Nature* **2018**, *560*, 336–339.
- (27) Yasuda, K.; Wang, X.; Watanabe, K.; Taniguchi, T.; Jarillo-Herrero, P. Stacking-engineered ferroelectricity in bilayer boron nitride. *Science* **2021**, *372*, 1458–1462, Publisher: American Association for the Advancement of Science.

Supporting information for “Mixed-stacking few-layer graphene as an elemental weak ferroelectric material”

Aitor Garcia-Ruiz,^{*,†,‡} Vladimir Enaldiev,^{†,‡} Andrew McEllistrim,^{†,‡} and
Vladimir I. Fal’ko^{†,‡,¶}

[†]*School of Physics and Astronomy, University of Manchester, Oxford Road, Manchester, M13
9PL, UK*

[‡]*National Graphene Institute, University of Manchester, Oxford Road, Manchester, M13 9PL, UK*

[¶]*Henry Royce Institute for Advanced Materials, University of Manchester, Oxford Road,
Manchester, M13 9PL, UK*

E-mail: altor.garcia-ruiz@manchester.ac.uk

Hamiltonian of rhombohedral graphite with a twin boundary

To construct the Hamiltonian of rhombohedral graphite with a twin-boundary fault, we incorporate all possible couplings described in Figure 1 of the main text. In the basis of A and B sublattice amplitudes and from the bottommost to the topmost layers, $\{\psi_{\beta,\mathbf{p}}^{A_1}, \psi_{\beta,\mathbf{p}}^{B_1}, \dots, \psi_{\beta,\mathbf{p}}^{B_{n+m+3}}\}$, this Hamil-

tonian takes the form

$$\begin{aligned}
\mathcal{H} &= \begin{pmatrix} H_g^s & V & W & \dots & 0 & \dots & 0 & 0 & 0 \\ V^\dagger & H_g^b & V & \dots & 0 & \dots & 0 & 0 & 0 \\ W^\dagger & V^\dagger & H_g^b & \dots & 0 & \dots & 0 & 0 & 0 \\ \vdots & \vdots & \vdots & \ddots & \vdots & \vdots & \vdots & \vdots & \vdots \\ 0 & 0 & 0 & \dots & \mathcal{H}_{ABA} & \dots & 0 & 0 & 0 \\ \vdots & \vdots & \vdots & \dots & \vdots & \ddots & \vdots & \vdots & \vdots \\ 0 & 0 & 0 & \dots & 0 & \dots & H_g^b & V^\dagger & W^\dagger \\ 0 & 0 & 0 & \dots & 0 & \dots & V & H_g^b & V^\dagger \\ 0 & 0 & 0 & \dots & 0 & \dots & W & V & H_g^s \end{pmatrix}, \quad (1) \\
H_g^s &= H_g + \begin{pmatrix} \Delta' & 0 \\ 0 & 0 \end{pmatrix}, \quad H_g^b = H_g + \Delta' \hat{1}_2, \quad H_g = v \begin{pmatrix} 0 & \pi_\xi^* \\ \pi_\xi & 0 \end{pmatrix}, \\
V &= \begin{pmatrix} -v_4 \pi_\xi & \gamma_1 \\ -v_3 \pi_\xi^* & -v_4 \pi_\xi \end{pmatrix}, \quad W = \begin{pmatrix} 0 & 0 \\ \gamma_2/2 & 0 \end{pmatrix}, \quad \pi_\xi \equiv \xi p_x + i p_y, \\
\mathcal{H}_{ABA} &= \begin{pmatrix} H_g^b & V & \tilde{W} \\ V^\dagger & H_g^b - \sigma_z \Delta' & V^\dagger \\ \tilde{W}^\dagger & V & H_g^b \end{pmatrix}, \quad \tilde{W} = \begin{pmatrix} \gamma_5/2 & 0 \\ 0 & \gamma_2/2 \end{pmatrix},
\end{aligned}$$

where we introduce the Sloczewski-Weiss-McClure (SWMcC) parameters^{???}, $v \approx 1.02 \cdot 10^6$ m/s, $\gamma_1 = 390$ meV, $v_3 \approx 0.1v$, $v_4 \approx 0.022v$, $\Delta' = 25$ meV, $\gamma_2 = -17$ meV and $\gamma_5 = 38$ meV[?], and $\xi = \pm 1$ is the valley index.

Hamiltonian of tetralayer graphite with a marginally twisted interface

Local stacking characterised by an interlayer offset, \mathbf{r}_0 at the twsited interface. The following Hamiltonians generalise those derived in Ref.[?]. For 2AB+2BA, Hamiltonian reads

$$\mathcal{H}_{AB+BA} = \begin{pmatrix} H_g^s & V & \mathcal{W}_{AB+1}(\mathbf{r}_0) & 0 \\ V^\dagger & H_g^s - \sigma_z \Delta' + \mathcal{E}_b & \mathcal{V}(\mathbf{r}_0) & \mathcal{W}_{1+BA}(\mathbf{r}_0) \\ \mathcal{W}_{AB+1}^\dagger(\mathbf{r}_0) & \mathcal{V}^\dagger(\mathbf{r}_0) & H_g^s - \sigma_z \Delta' + \mathcal{E}_t & V^\dagger \\ 0 & \mathcal{W}_{1+BA}^\dagger(\mathbf{r}_0) & V & H_g^s \end{pmatrix} \quad (2)$$

$$\begin{aligned} \mathcal{V}(\mathbf{r}_0) &= \sum_{j=0}^2 \left\{ \left[\frac{\gamma_1}{3} - \frac{2v_4 \hbar}{3K} \mathbf{k} \cdot \mathbf{K}_\xi^{(j)} \right] \begin{pmatrix} 1 & e^{i\xi \frac{2\pi}{3} j} \\ e^{-i\xi \frac{2\pi}{3} j} & 1 \end{pmatrix} \right. \\ &\quad \left. + \frac{\xi 2(v_3 - v_4) \hbar}{3K} [\mathbf{k} \times \mathbf{K}_\xi^{(j)}]_z \begin{pmatrix} 0 & ie^{i\xi \frac{2\pi}{3} j} \\ -ie^{-i\xi \frac{2\pi}{3} j} & 0 \end{pmatrix} \right\} e^{-i\mathbf{K}_\xi^{(j)} \cdot \mathbf{r}_0}, \\ \mathcal{W}_{AB+1}(\mathbf{r}_0) &= \frac{1}{6} \sum_{j=0}^2 \begin{pmatrix} \gamma_5 e^{-i\xi \frac{2\pi}{3} j} & \gamma_5 \\ \gamma_2 e^{+i\xi \frac{2\pi}{3} j} & \gamma_2 e^{-i\xi \frac{2\pi}{3} j} \end{pmatrix} e^{-i\mathbf{K}_\xi^{(j)} \cdot \mathbf{r}_0}, \\ \mathcal{W}_{1+BA}(\mathbf{r}_0) &= \frac{1}{6} \sum_{j=0}^2 \begin{pmatrix} \gamma_5 e^{+i\xi \frac{2\pi}{3} j} & \gamma_2 e^{-i\xi \frac{2\pi}{3} j} \\ \gamma_5 & \gamma_2 e^{+i\xi \frac{2\pi}{3} j} \end{pmatrix} e^{-i\mathbf{K}_\xi^{(j)} \cdot \mathbf{r}_0}, \\ \mathcal{E}_{b/t} &= \frac{2\Delta'}{3} \hat{1}_2 + \frac{\Delta'}{9} \sum_{\mathbf{G}} e^{i\mathbf{G} \cdot \mathbf{r}_0} \begin{pmatrix} 1 + e^{\pm i\mathbf{G} \cdot \boldsymbol{\tau}_B} & 0 \\ 0 & 1 + e^{\mp i\mathbf{G} \cdot \boldsymbol{\tau}_B} \end{pmatrix}, \end{aligned}$$

where we introduce K-valleys momenta, $\mathbf{K}_\xi^{(j)} = \xi K [\cos(j2\pi/3), -\sin(j2\pi/3)]$, with $K = 4\pi/3a$ ($a \approx 2.46 \text{ \AA}$ is the lattice constant of graphene). We note that for $\mathbf{r}_0 = (0, a/\sqrt{3})$ and $\mathbf{r}_0 = (0, -a/\sqrt{3})$, Eq. (2) transforms to the Hamiltonian of ABAC and ABCB, respectively. Likewise,

the Hamiltonian of monolayer-twisted-trilayer structures is given by

$$\mathcal{H}_{\text{ABA}+1} = \begin{pmatrix} H_g^s & V & \tilde{W} & 0 \\ V^\dagger & H_g^b - \sigma_z \Delta' & V^\dagger & \mathcal{W}_{\text{BA}+1}(\mathbf{r}_0) \\ \tilde{W}^\dagger & V & H_g^s + \mathcal{E}_b & \mathcal{V}(\mathbf{r}_0) \\ 0 & \mathcal{W}_{\text{BA}+1}^\dagger & \mathcal{V}^\dagger(\mathbf{r}_0) & H_g + \mathcal{E}_t \end{pmatrix}, \quad (3a)$$

$$\mathcal{H}_{\text{ABC}+1} = \begin{pmatrix} H_g^s & V & W & 0 \\ V^\dagger & H_g^b & V & \mathcal{W}_{\text{AB}+1}(\mathbf{r}_0) \\ W^\dagger & V & H_g^s - \sigma_z \Delta' + \mathcal{E}_b & \mathcal{V}(\mathbf{r}_0) \\ 0 & \mathcal{W}_{\text{AB}+1}^\dagger(\mathbf{r}_0) & \mathcal{V}^\dagger(\mathbf{r}_0) & H_g + \mathcal{E}_t \end{pmatrix}, \quad (3b)$$

$$\mathcal{W}_{\text{BA}+1}(\mathbf{r}_0) = \frac{1}{6} \sum_{j=0}^2 \begin{pmatrix} \gamma_2 e^{+i\xi \frac{2\pi}{3} j} & \gamma_2 e^{-i\xi \frac{2\pi}{3} j} \\ \gamma_5 & \gamma_5 e^{+i\xi \frac{2\pi}{3} j} \end{pmatrix} e^{-i\mathbf{K}_\xi^{(j)} \cdot \mathbf{r}_0}.$$

Convergence analysis

In our analysis, we compute the electron density in each layer by brute-force diagonalisation of the Hamiltonian (1) for a sufficiently dense grid of points in reciprocal space within a circular area with cut-off wavevector, k_c . For each nABAm film, as k_c increases, the ferroelectric polarisation converges to a P_z -value, displayed below in the left panel of Fig. 2 (c). To illustrate that this value of the cut-off is large enough, we consider behaviour of P_z versus k_c for two characteristic structures: 4ABA and 4ABA3, shown in Fig. 1.

The low-energy dispersion of 4ABA graphite film features a couple of flat bands and a pair of Dirac dispersive bands [see inset in Fig. 1 (a)]. The former, strongly localised at the bottom and twin boundary layers, induces a polarisation in the positive z -direction, while the latter, hybridising with deeper bands, contributed to P_z in negative direction of z -axis. As shown Fig. 1 (a), it is necessary to sample an area of $5 \cdot 10^{-2} \text{ \AA}^{-2}$ (or a value for the cut-off energy of $\sim -0.13 \text{ eV}$) to reach convergence.

In contrast, the low-energy dispersion of 4ABA3 exhibits two pairs of flat bands [see inset in

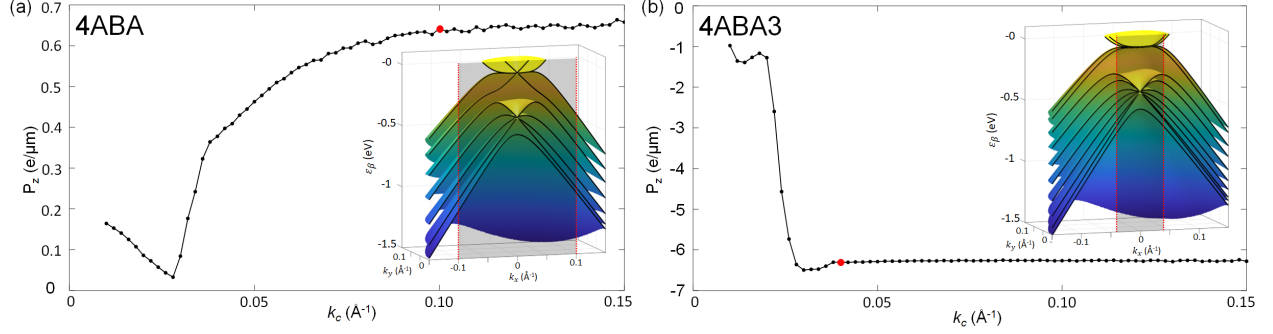


Figure 1: Value for the ferroelectric polarisation, P_z , as a function of the radius of the circle centred at \mathbf{K}_{\pm} in reciprocal space, k_c taken to compute the electron density in each layer, for 4ABA (a) and 4ABA3 (b) tetralayer graphene. For the latter, it suffices to sample the area on which flat bands extend to obtained a converged value.

Fig. 1 (b)], with a much stronger localisation at the twin boundary and non-dimer site of surface layer, that are well-separated from the rest continuum of the deep-energy states. In this case P_z converges at smaller area of reciprocal space, about $5 \cdot 10^{-3} \text{ \AA}^{-2}$ (or a value for the cut-off energy of $\sim -0.07 \text{ eV}$), which corresponds to the region of high density of states of the flat bands.

Self-consistent implementation of screening

Here, we extend the above-described SWMcC model to incorporate the effects of internal electric fields produced by the charge redistribution. These fields produce an energy offset in each layer, which can be captured in our model by adding a term $\epsilon_i \hat{1}_2$ to the i -th diagonal block of the Hamiltonians in Eqs. (1), (2) and (3) using the formula[?]

$$\epsilon_i - \epsilon_{i-1} = \frac{e^2 d}{2\epsilon_0} \left[(n_i - n_{i-1}) \frac{1 + \epsilon_z^{-1}}{2} + \sum_{j>i} n_j \epsilon_z^{-1} - \sum_{j'<i-1} n_{j'} \epsilon_z^{-1} \right], \quad (4)$$

with $d \approx 3.35 \text{ \AA}$ being the interlayer distance in graphene stacks, $\epsilon_z \approx 2.6$ [?] the relative permittivity of graphene. We determine the Fermi level for neutral structures, and calculate the charge redistribution across the layers, taking into account only the eigenvectors associated to states below the Fermi level. Because the charge densities n_i also depend implicitly on the on-layer potentials,

the expression in Eq. (4) needs to be solved self-consistently. In the first iteration, we set all on-layer energies to zero, $\epsilon_i^{(0)} = 0$, which gives the value of polarisation for the unscreened system, P_z^u . In each iteration, we use Eq. (4) to compute a new set of on-layer energies, $\tilde{\epsilon}_i^{(n)}$, which are used to update the value employed in the following iteration using

$$\epsilon_i^n = \eta \tilde{\epsilon}_i^{(n)} + (1 - \eta) \epsilon_i^{(n-1)},$$

where η determines the fraction of the value for the on-layer energies that is updated in each iteration, and was taken to be $4 \cdot 10^{-4}$ in our work. This linear-mixing algorithm is necessary in a broad range of self-consistent methods to avoid overshooting[?].

In Figs. 2(a) and 2(b), we show the value of P_z and electron densities in each layer as a function of the iteration for 1ABA and 4ABA3 films, highlighting importance of self-consistent calculations. Histograms in Fig. 2(c) show comparison of P_z values for mABAn films with less than 8 layers computed with (right) and without (left) account of self-consistent screening. We also note that our results strongly depend on the input parameters, and suggest that measuring P_z in these systems could be an experimental route to narrow down the possible values of the SWMcC parameters.

Analysis of parametric dependence

Equation (3) of the main text is based on the analysis shown in Fig. 3, where each panel represents dependence of P_z^u of ABCB tetralayer graphene on one of the SMWcC parameters. The blue dots are numerically computed values of P_z^u and the red lines are the linear interpolations, which we use to obtain the coefficients $\mathcal{X}_{4,D,2,5}$. We observe the linear dependence of P_z on the symmetry-breaking parameters v_4 , Δ' , γ_2 and γ_5 . The middle and rightmost panels of Fig. 3 (a), shows the dependence on γ_1 and v , when v_4 is kept as the only non-zero electron-hole symmetry-breaking parameter, which is proportional to $\gamma_1 |\gamma_1| \times v^{-3}$, respectively. Likewise, in the same panels of Figs. 3 (b), (c) and (d), we demonstrate that P_z^u as the power law $|\gamma_1| \times v^{-2}$ when Δ' , γ_2 and γ_5

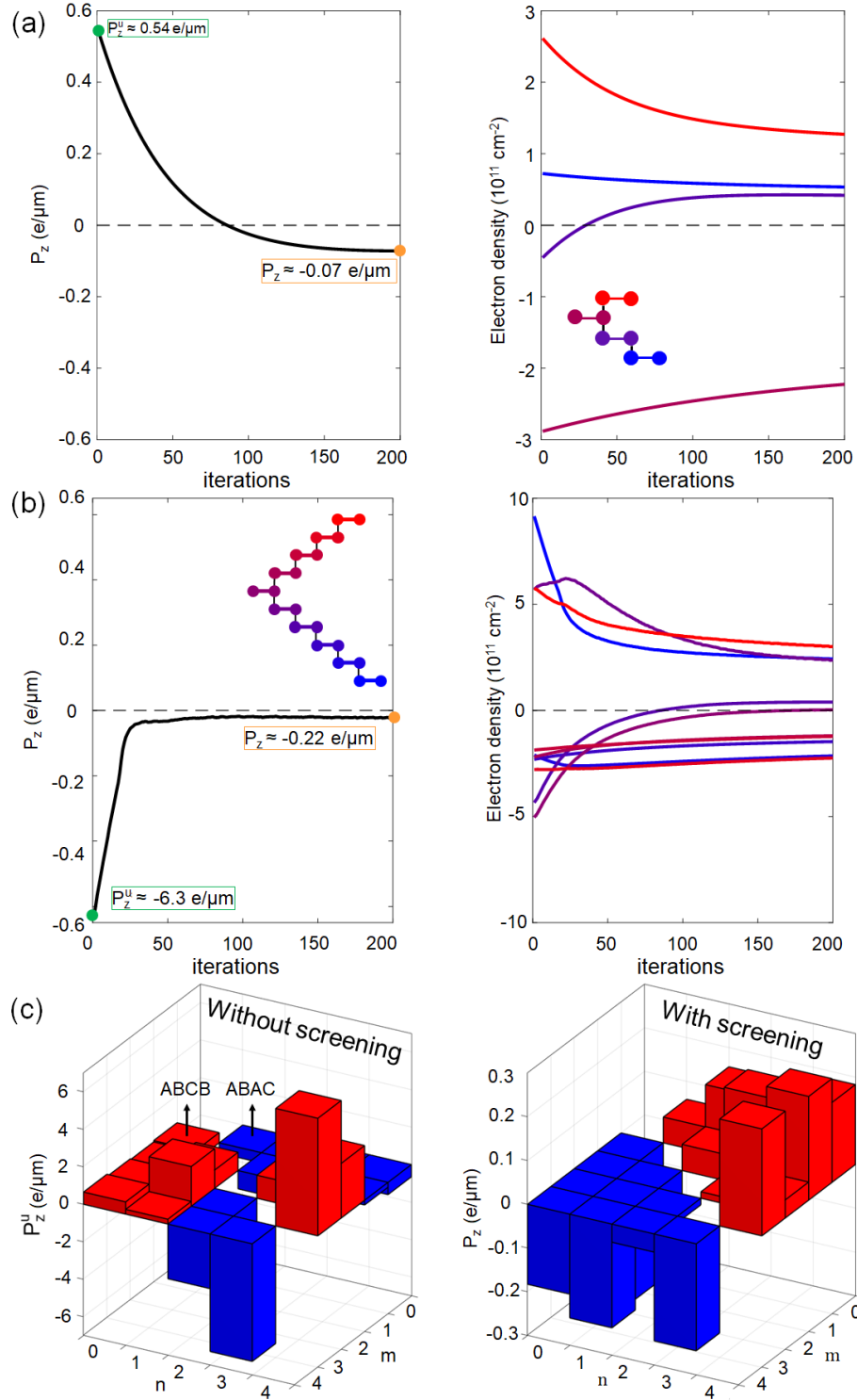


Figure 2: Convergence analysis of P_z and n_i for (a) 1ABA and (b) 4ABA3 films. The latter evidences that, for larger films, electron charge primarily redistributes to the surface and twin boundary layers. (c) Electric polarisation of mABAn, P_z^u (P_z), displayed in the form of a histogram, using a model that neglects (accounts for) screening effects of electron-density redistribution.

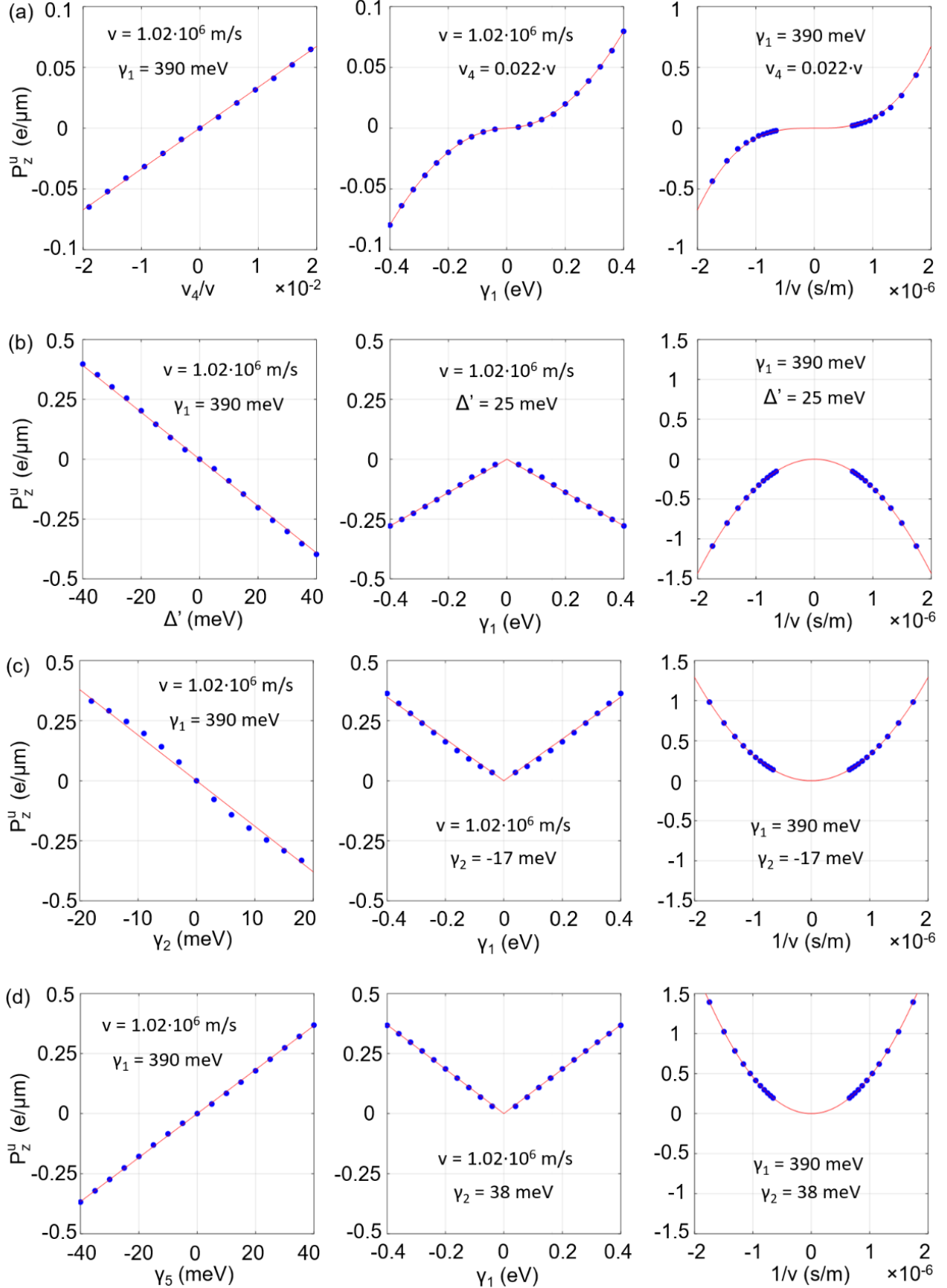


Figure 3: Numerical values (blue points) and fitting curves (red) computed to support the parametric dependence of the first, second, third and fourth terms in Eq. (2) in the main text are analysed in the triad of panels (a), (b), (c) and (d), respectively, for ABCB tetralayer graphene. In the leftmost panels, we demonstrate the linear dependence of each SWMCC parameter that induces ferroelec-

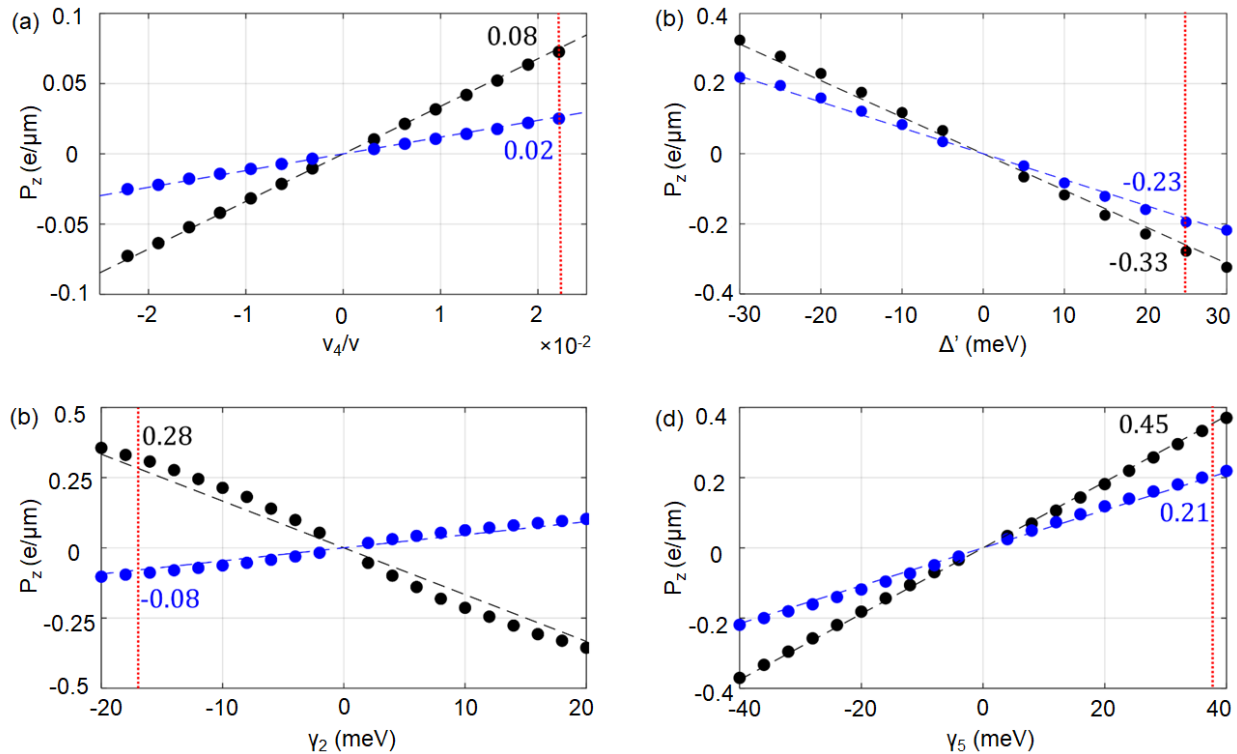


Figure 4: Dependence of P_z^u (black) and P_z (blue) as a function of each individual SWMcC parameter responsible for electron-hole asymmetry. Vertical red dotted lines lie on the values given in³, which we use in our work. Adding all the values where they intersect the black and blue interpolating lines amounts approximately the value for P_z^u and P_z obtained using the full SWMcC model, and shown as the first and last values in Fig. 2(a).

are kept as the only non-zero parameters, respectively.

In Fig. 4, we extend analysis of P_z when effect of self-consistent screening is taken into account. In particular, we compare the leftmost panels of Fig. 3 using a model with (blue dots) and without (black dots) the effects of screening, and demonstrate that, while \mathcal{X}_4 , \mathcal{X}_D and \mathcal{X}_5 reduce their values by a factor of ~ 4 , 1.4 and 2.2, respectively, the coefficient \mathcal{X}_2 changes sign. As stated in the main text, this peculiar behaviour plays a prominent role in the change of sign of polarisation, being $P_z^u \approx 0.54 \text{ e}/\mu\text{m}$ in the unscreened model and $P_z \approx -0.07 \text{ e}/\mu\text{m}$ in the screened model [see Fig. 2(a)]. It is also worth mentioning that adding the individual contributions to P_z (or P_z^u) from the four symmetry-breaking terms amounts approximately to the to computed using the full SWMcC model with (without) the account for screening effects.

Lattice relaxation in twisted tetralayer structures

To describe lattice reconstruction of moiré superlattice formed at the twisted interface we introduce in-plane displacement fields $\mathbf{u}_{t/b}$ acting in top/bottom stacks. For 3+1 tetralayers top (bottom) stack consists of 1 (3) graphene layers, while for 2+2 structures the top/bottom stacks are graphene bilayers. To find $\mathbf{u}_{t/b}$ we minimize sum of elastic, $U = \sum_{l=t,b} \left[(\lambda_l/2) \left(u_{ii}^{(l)} \right)^2 + \mu_l u_{ij}^{(l)} u_{ji}^{(l)} \right]$, and local adhesion, $W(\mathbf{r}_0 = \theta \hat{z} \times \mathbf{r} + \mathbf{u}^{(t)} - \mathbf{u}^{(b)})$, energies over supercell with periodicity of moiré superlattice given by twist angle θ expanding the displacement fields into Fourier series[?]: $\mathbf{u}_{t/b} = \sum_{\{\lambda\}, j=0,1,2} \left[\hat{R}_{2\pi j/3} \mathbf{u}_{\{\lambda\}}^{(t/b)} \right] \sin \left(\mathbf{g}_{\{\lambda\}}^{(j,+)} \mathbf{r} \right)$ with $\mathbf{g}_{\{\lambda\}}^{(j,+)} = \theta \mathbf{G}_{\{\lambda\}}^{(j,+)} \times \hat{z}$ and \hat{R}_ϕ is counter clock-wise rotation on angle ϕ around \hat{z} . Obtained values of non-negligible Fourier amplitudes are listed in Table 1. In calculations, elastic moduli of top/bottom stacks were determined by those of graphene $\lambda_G = c_0 Y \nu / (1 + \nu)(1 - 2\nu)$, $\mu_G = c_0 Y / 2(1 + \nu)$ (with Young module, $Y = 1 \text{ TPa}$, and Poisson ratio, $\nu = 0.19$ [?]), multiplied by the number of graphene layers in each stack. For the adhesion energy at twisted interface we used the following expression^{??}: $W(\mathbf{r}_0) = \sum_{\Lambda=1,2,3} w_\Lambda \sum_{j=0,1,2} \cos \left(\mathbf{G}_\Lambda^{(j,+)} \cdot \mathbf{r}_0 \right)$ with $w_1 = 0.775 \text{ meV}/\text{Å}^2$, $w_2 = -0.071 \text{ meV}/\text{Å}^2$, $w_3 = -0.018 \text{ meV}/\text{Å}^2$.

Table 1: Main non-zero Fourier series coefficients (in \AA) of displacement fields describing reconstruction in twistrionic tetralayers 3ABA+1, 3ABC+1 and 2AB+2BA structures with $\theta = 0.05^\circ$, which were used in Fig. 2 of the main manuscript.

$\{\lambda_1, \lambda_2\}$	3AB(A/C)+1		2AB+2BA
	(1L) $u_{\lambda_1, \lambda_2}^{(t)}$	(3L) $u_{\lambda_1, \lambda_2}^{(b)}$	$u_{\lambda_1, \lambda_2}^t (= -u_{\lambda_1, \lambda_2}^b)$
1, 0	(0.2898, 0.1687)	-(0.0979, 0.0565)	(0.1938, 0.1119)
2, 0	(0.1394, 0.0797)	-(0.0463, 0.0265)	(0.0910, 0.0526)
3, 0	(0.0875, 0.5089)	-(0.0292, 0.0169)	(0.0573, 0.0330)
4, 0	(0.0606, 0.0349)	-(0.0202, 0.0116)	(0.0389, 0.0225)
5, 0	(0.0428, 0.0247)	-(0.0143, 0.0082)	(0.0264, 0.0153)
6, 0	(0.0322, 0.0185)	-(0.0107, 0.0062)	(0.0201, 0.0116)
7, 0	(0.0227, 0.0132)	-(0.0076, 0.0044)	(0.0130, 0.0075)
8, 0	(0.0191, 0.0109)	-(0.0064, 0.0037)	(0.0121, 0.0070)